

Impact of the honeycomb spin-lattice on topological magnons and edge states in ferromagnetic 2D skyrmion crystals

Doried Ghader*¹ and Bilal Jabakhanji¹

¹ College of Engineering and Technology, American University of the Middle East, Egaila 54200, Kuwait

*doried.ghader@aum.edu.kw

Abstract

Magnons have been intensively studied in two-dimensional (2D) ferromagnetic (FM) skyrmion crystals (SkXs) stabilized on Bravais lattices, particularly triangular and square lattices, where the first two magnon gaps are topologically trivial and do not support topological edge states (TESs). Meanwhile, the third gap can host TESs, which may be trivialized through field-induced topological phase transitions (TPTs), enabling controlled magnonic edge transport. However, the magnon topology in non-Bravais spin lattices remains largely unexplored. In this work, we theoretically investigate the influence of the honeycomb lattice structure on magnon band topology and associated TESs in FM SkXs, employing realistic parameters for monolayer CrI_3 and $CrBr_3$. We reveal unique magnonic topological features arising specifically from the honeycomb lattice. Characteristic magnon modes, such as elliptical and triangular distortion modes, acquire nontrivial Chern numbers, contrasting their trivial counterparts in triangular-based SkXs. Moreover, the second magnon gap in honeycomb-based SkXs consistently hosts TESs at low magnetic fields, unlike triangular SkXs. These TESs can be trivialized above a critical magnetic field. Conversely, the third gap is generally topological at higher magnetic fields but becomes topological at low fields only when the SkX periodicity falls below a critical threshold dependent on Dzyaloshinskii–Moriya interaction (DMI) strength and magnetic anisotropy. Our study further demonstrates a rich magnonic topological phase diagram accessible by magnetic fields, potentially enabling selective control of low-energy chiral edge modes. These findings underscore the pivotal role of lattice geometry in shaping the topology of magnons in noncollinear spin textures.

1. Introduction

Recent theoretical studies [1–11] have established skyrmion crystals (SkXs) [12–14] as exceptional platforms for exploring topological magnonics and magnon spintronics. In these noncollinear spin textures, magnons (the quanta of spin waves) propagate within an effectively nontrivial magnetic superlattice, experiencing emergent fields generated by the spatially varying magnetization [5,8,15–20]. This scenario profoundly impacts the magnon band structure, resulting in nonzero Berry curvatures, quantized Chern numbers, and topological band gaps. A significant consequence of this nontrivial band topology is the emergence of chiral edge states localized at the boundaries of the SkX [1,4,5,10]. These unidirectional magnon modes facilitate spin and heat transport without backscattering, potentially enabling low-dissipation information transfer. Experimentally, Akazawa et al. provided compelling evidence of a topological thermal Hall signal in the SkX phase of the insulating polar magnet GaV_4Se_8 , consistent with magnonic edge-state transport [21]. Furthermore, the theoretical prediction of emergent magnon Landau levels was dramatically confirmed through inelastic neutron scattering experiments on $MnSi$ in its skyrmion phase [18]. These experimental findings strongly support theoretical models, directly confirming that noncollinear SkX backgrounds give rise to robust topological magnon band structures.

Considerable effort has been devoted to investigating the magnon band topology and edge states in SkXs on the two-dimensional (2D) triangular Bravais spin-lattice [4–7,9,22]. In particular, Néel-type ferromagnetic (FM) SkXs on the triangular lattice have been shown to exhibit gapped magnon bands, whose modal characteristics can be identified by examining spin precession patterns at the Brillouin zone (BZ) center [4,5]. At minimal magnetic field, the third magnon band corresponds to a counterclockwise (CCW) circular mode, where spins precess collectively around each skyrmion core. In contrast, the fourth band corresponds to a breathing mode characterized by expansion and contraction of skyrmions. The two lowest-energy magnon bands are topologically trivial, while the CCW and breathing modes each carry a Chern number of $C = 1$. Consequently, topologically protected chiral magnonic edge states emerge within the CCW-breathing gap at minimal magnetic field. Díaz et al. [4] demonstrated that increasing the magnetic field eventually closes and subsequently reopens the CCW-breathing gap at a critical field, inducing a topological phase transition (TPT). Following this TPT, the CCW-breathing gap becomes topologically trivial, and the associated topological edge states (TESSs) disappear. Their analysis also indicated that the evolution of the CCW-breathing gap under a magnetic field is a general feature, independent of

the strength of the Dzyaloshinskii–Moriya interaction (DMI). These theoretical insights highlight how an external magnetic field can serve as an effective tuning parameter, enabling on-demand switching of magnonic edge transport through controlled manipulation of band topology, thus providing a practical route to externally modulate magnonic currents in SkXs.

The magnon excitation spectrum in 2D SkXs is expected to reflect the underlying spin-lattice geometry, analogous to simpler collinear FM cases. A 2D collinear ferromagnet on a triangular Bravais lattice supports a single magnon band, with a bandwidth determined primarily by its coordination number ($z = 6$). By contrast, the honeycomb lattice is a non-Bravais, bipartite structure with two sites per unit cell and a lower coordination number ($z = 3$). Consequently, a collinear ferromagnet on the honeycomb lattice hosts two magnon bands (acoustic and optical), which intersect at Dirac nodal points located at the BZ corners in the absence of symmetry-breaking interactions. The reduced coordination number of the honeycomb lattice decreases the magnon bandwidth relative to that of the triangular lattice. Furthermore, the honeycomb geometry enables richer topological magnon phenomena. For instance, the inclusion of next-nearest-neighbor (NNN) DMI, permitted by honeycomb-lattice symmetry, opens gaps at the Dirac magnon nodes, resulting in nonzero Chern numbers and chiral magnonic edge states [23–27]. In contrast, a triangular spin-lattice collinear ferromagnet, due to having only a single magnon branch, inherently lacks such band-crossing topology and thus cannot support a nonzero Chern invariant or analogous topological edge modes.

Given the profound impact of lattice geometry on the magnon spectrum in 2D collinear FM phases, it is anticipated that the honeycomb lattice geometry in the SkX phases could enable magnonic band topologies and field-driven TPTs beyond those realizable in simpler triangular SkXs. Indeed, several 2D van der Waals magnets (e.g., CrI_3 , CrBr_3 , $\text{Cr}_2\text{Ge}_2\text{Te}_6$) naturally exhibit honeycomb spin-lattice structures [26,28–37]. Nonetheless, material-specific studies of magnons in 2D skyrmion crystals remain scarce, despite their pivotal role at the intersection of two forefront research fields: van der Waals 2D magnetism and skyrmion-based topological magnonics.

In this work, we theoretically investigate magnons in Néel-type FM SkXs on 2D honeycomb spin-lattices. We consider two experimentally relevant parameter sets for CrI_3 (Models 1 [27] and 2 [25]) and a third for CrBr_3 (Model 3 [38]), which differ in intrinsic magnetic parameters. This analysis allows us to draw robust and general conclusions.

Following previous studies [1,2,4,5,39], we stabilize skyrmions via interfacial NN DMI. The skyrmion crystals are simulated using stochastic Landau–Lifshitz–Gilbert (sLLG) equations across a broad range of NN DMI strengths. We introduce a numerical scheme to systematically study the evolution and deformation of SkXs induced by incremental increases in magnetic field throughout the entire stability region of the skyrmion phase.

Our results show that the magnon topology in honeycomb-based SkXs differs fundamentally from the triangular-lattice SkXs extensively studied in previous literature. Characteristic magnon modes (e.g., CW, CCW, breathing, elliptical distortion (ED), and triangular distortion) exhibit distinct Chern numbers compared to their triangular-lattice counterparts. Consequently, the second magnon gap in honeycomb-based SkXs robustly hosts TESs at low magnetic fields, a feature absent in triangular-based systems. This TES presence in the second gap is a general attribute of honeycomb FM SkXs, independent of material parameters or SkX periodicity. These TESs are consistently trivialized through TPTs, occurring upon closing and reopening the second gap at critical magnetic fields. Notably, the second gap closure occurs exactly once within the entire stability field range, thus restricting TES presence to low magnetic fields.

In contrast, the third magnon gap exhibits a more intricate, periodicity-dependent (equivalently, interfacial DMI-dependent) behavior in honeycomb-based SkXs. We identify a critical SkX periodicity, corresponding to a threshold NN DMI, that separates two distinct behaviors of the third gap at low magnetic fields. This critical periodicity increases as single-ion magnetic anisotropy (SIMA) decreases. Only when the periodicity is smaller than or equal to this critical value is the third gap topological at low magnetic fields. Furthermore, unlike the second gap, the third gap may experience multiple field-induced closures and reopenings, turning TESs on and off. Nevertheless, the third gap always hosts TESs within a relatively high magnetic-field range, regardless of material parameters or periodicity.

Overall, these findings demonstrate that honeycomb-based SkXs support richer low-energy magnonic topological edge states compared to triangular-lattice SkXs. Specifically, both second and third magnon band gaps in honeycomb-based systems can host TESs, providing distinct and spectrally separated channels suited for frequency-multiplexed magnon transport at low energies. These topological channels can be individually activated or deactivated at distinct critical magnetic fields, enabling magnetic-field-tunable multi-channel transport. Thus, our study underscores the

significant potential of lattice geometry for engineering low-energy topological magnon transport in skyrmion-based systems.

2. Modeling the SkX

We consider a spin Hamiltonian on a 2D honeycomb lattice incorporating FM Heisenberg exchange, SIMA, and both NN and NNN DMIs. The NN DMI is of interfacial origin [1,2,4,5,39], while the NNN DMI arises intrinsically and has been observed experimentally in several honeycomb 2D magnets [24,25,27,40]. The Hamiltonian is given by

$$\mathcal{H} = -J \sum_{\langle i,j \rangle} \mathcal{S}_i \cdot \mathcal{S}_j - \sum_{\langle i,j \rangle} \mathbf{d}_{ij} \cdot \mathcal{S}_i \times \mathcal{S}_j - \mathcal{A} \sum_i (\mathcal{S}_i^z)^2 - \sum_{\langle\langle i,j \rangle\rangle} \mathbf{D}_{ij} \cdot \mathcal{S}_i \times \mathcal{S}_j - B \sum_i \mathcal{S}_i^z \quad (1)$$

Here, \mathcal{S}_i denotes the spin operator at site i of the honeycomb lattice. The first three terms describe the FM NN Heisenberg exchange with strength J , the interfacial-type NN DMI with vectors \mathbf{d}_{ij} ($d = |\mathbf{d}_{ij}|$), and the SIMA with strength \mathcal{A} . The fourth term represents the intrinsic NNN DMI with strength $D = |\mathbf{D}_{ij}|$, while the last term accounts for the Zeeman coupling due to an external magnetic field B applied along the z -axis, normal to the honeycomb lattice. The vectors \mathbf{d}_{ij} and \mathbf{D}_{ij} define the chiral directions of the NN and NNN DMIs, respectively (see Supplementary Figure S1).

To enable a general analysis of magnon topology and edge states in honeycomb-based SkXs, we normalize all energy scales with respect to J , reducing the parameter space to D/J and \mathcal{A}/J . We study three representative models derived from experimental investigations of magnon excitations in the collinear FM phases of monolayer CrI_3 and $CrBr_3$, in the absence of NN DMI. These models, summarized in Table 1, span different values of the intrinsic parameters D/J and \mathcal{A}/J , providing a suitable framework for assessing the impact of SIMA and intrinsic DMI on the magnonic topology of honeycomb-based SkXs.

	Material	Parameters
Model 1 [27]	CrI_3	$J_1 = 2.13 \text{ meV}$, $D_1 = 0.19 \text{ meV}$, $\mathcal{A}_1 = 0.22 \text{ meV}$
Model 2 [25]	CrI_3	$J_2 = 2.11 \text{ meV}$, $D_2 = 0.09 \text{ meV}$, $\mathcal{A}_2 = 0.123 \text{ meV}$
Model 3 [38]	$CrBr_3$	$J_3 = 1.48 \text{ meV}$, $D_3 = 0$, $\mathcal{A}_3 = 0.029 \text{ meV}$

Table 1. Magnetic parameters for Models 1, 2 and 3, representing different experimental estimates for CrI_3 and $CrBr_3$ in their collinear FM phases. Here, J is the FM Heisenberg exchange, D is the next-nearest-neighbor Dzyaloshinskii–Moriya interaction, and \mathcal{A} is the single-ion magnetic anisotropy.

We simulated the ground state for the three models using the sLLG equations within the Vampire software package [41]. FM (Néel-type) SkXs were observed above a threshold NN DMI, which increases with \mathcal{A} . For DMI strengths above the threshold, we first determined the minimal magnetic field B_{min} required to stabilize the SkX. In this calculation, simulations were initialized from random spin configurations at high temperatures and then gradually cooled to near zero temperature. At B_{min} , the skyrmions are densely packed, forming a triangular lattice. It should be noted, however, that the SkXs generated by Vampire are not perfectly ordered due to the random nucleation of DMI-induced skyrmions [42–44]. Nevertheless, idealized SkX configurations can be generated based on the Vampire results using suitable analytical functions [6]. Once the SkX is stabilized, the magnetic field B is incrementally increased to study the evolution of the texture, with the temperature maintained near zero. As B increases, individual skyrmions gradually shrink in size while remaining pinned to their original lattice sites, thus preserving the triangular SkX structure and its BZ. Eventually, beyond a critical magnetic field B_{max} , the skyrmions are gradually annihilated, and the system gradually transitions into a uniform ferromagnetic state. Determining the skyrmion size as a function of the magnetic field is essential for understanding its impact on magnon excitations. We develop a practical method to extract the field-dependent effective skyrmion width from the integrated out-of-plane spin density of a skyrmion crystal. At the minimal magnetic field, the densely packed SkX features hexagonal skyrmions with initial width w_0 and area $A_0 = \frac{\sqrt{3}}{2} w_0^2$ (Supplementary Figure S2a). Notably, w_0 defines the inter-skyrmion distance and hence matches the SkX periodicity (Supplementary Figure S2b). Let $S_0^z(\mathbf{r})$

denote the interpolated z-component of the spin field in this configuration. The corresponding out-of-plane spin density is

$$\eta_0 = \frac{1}{A_0} \iint_{A_0} S_0^z(\mathbf{r}) ds \quad (2a)$$

At an increased magnetic field $B > B_{min}$, each skyrmion shrinks and no longer occupies the entire unit cell (Supplementary Figure S2a). Assuming a self-similar deformation, the skyrmion at this field has width $w < w_0$ and area $A_s = \frac{\sqrt{3}}{2} w^2 < A_0$, while the remaining region corresponds to spins aligned along the z-direction. The new out-of-plane spin density is given by

$$\eta = \frac{1}{A_0} \iint_{A_0} S^z(\mathbf{r}) ds \quad (2b)$$

where $S^z(\mathbf{r})$ is the updated interpolation function at field B . Recognizing that $\iint_{A_s} S^z(\mathbf{r}) ds = \eta_0 A_s$, the updated density becomes

$$\eta = \frac{1}{A_0} \iint_{A_0 - A_s} 1 ds + \frac{1}{A_0} \iint_{A_s} S^z(\mathbf{r}) ds = 1 + \frac{A_s}{A_0} (\eta_0 - 1) \quad (2c)$$

Substituting $\frac{A_s}{A_0} = \frac{w^2}{w_0^2}$, we obtain the skyrmion width as a function of η

$$w = w_0 \sqrt{\frac{\eta - 1}{\eta_0 - 1}} \quad (2d)$$

In practice, we used *Mathematica* to analyze the spin textures obtained from Vampire sLLG simulations and numerically extracted $w(B)$ using Equations (2a), (2b), and (2d).

3. Magnon Hamiltonian for honeycomb-based ferromagnetic SkXs

We adopt a discrete Holstein–Primakoff bosonization scheme [1–3,5,45] to quantize the spin excitations, which is more suitable than continuum approaches [6] for the relatively small skyrmions appearing in the models under study. While this method has been extensively developed for triangular spin-lattice SkXs, we extend it here to treat SkXs on the two-sublattice honeycomb structure and include contributions arising from the NNN DMI. A brief overview of the theoretical framework is provided below, and full technical details can be found in the Supplementary Material.

In the noncollinear SkX state, each spin at lattice site i has a local orientation \mathbf{n}_i that differs from the global z -axis. To account for this, we perform a local spin-axis rotation at each site [46] to align the local spin quantization axis with the spin’s equilibrium orientation \mathbf{n}_i . This transformation maps the SkX onto an equivalent ferromagnetic state in the rotating frame. We then apply Holstein–Primakoff bosonization in this rotated frame, expressing the spin operators in terms of bosonic magnon creation (a_i^+, b_j^+) and annihilation (a_i, b_j) operators defined about the local ordered spin. Here, a_i and b_j denote magnon operators on sublattices A and B, respectively.

The magnetic unit cell of the SkX is defined as the cluster of spins forming a single skyrmion in the minimal-field configuration. For a skyrmion of width w_0 , this unit cell contains $N_s = w_0^2$ spins per sublattice (i.e., $2N_s$ spins in total). The skyrmion centers form a triangular Bravais lattice in real space, and thus, in momentum space, one can define a magnon Bloch wavevector (or momentum) \mathbf{k} in the SkX BZ, which is a mini-BZ relative to that of the atomic lattice.

After Fourier transforming the bosonic operators to momentum space, the quadratic magnon Hamiltonian takes the form,

$$\mathcal{H} = \frac{1}{2} \sum_{\mathbf{k}} \Psi^\dagger h(\mathbf{k}) \Psi \quad (3a)$$

with

$$h(\mathbf{k}) = \begin{pmatrix} X(\mathbf{k}) & Y(\mathbf{k}) \\ Y^\dagger(\mathbf{k}) & X^T(-\mathbf{k}) \end{pmatrix} \quad (3b)$$

and

$$\Psi^\dagger = (a_{\mathbf{k}1}^+ \ \dots \ a_{\mathbf{k}N}^+ \ \ b_{\mathbf{k}1}^+ \ \dots \ b_{\mathbf{k}N_s}^+ \ \ a_{-\mathbf{k}1} \ \dots \ a_{-\mathbf{k}N} \ \ b_{-\mathbf{k}1} \ \dots \ b_{-\mathbf{k}N_s}) \quad (3c)$$

In Equations (3), \mathbf{k} is a wavevector in the SkX BZ, and $h(\mathbf{k})$ is a $4N \times 4N$ matrix. The block matrices $X(\mathbf{k})$ and $Y(\mathbf{k})$ are each $2N \times 2N$, and they encode all relevant exchange, anisotropy, and DMI interactions, including the NNN DMI. The explicit forms of these matrix elements are given in the Supplementary Material.

The matrix $h(\mathbf{k})$ is diagonalized using a standard bosonic Bogoliubov transformation following Colpa's method [47]. This procedure yields the magnon band energies E_n ($n = 1, 2, \dots$) and corresponding eigenvectors, from which one can compute the Berry curvature and Chern number associated with each band. In particular, the Berry curvatures and Chern numbers are calculated using the numerical method developed by Fukui *et al.* [48]. Extensive details on the implementation of this method for magnonic band structures can be found in previous works [6,49,50], and are omitted here for brevity.

4. Magnon bands, topology, and edge states

Magnons, being bosonic quasiparticles, primarily occupy the lowest-energy states. Accordingly, the low-energy bands and gaps are the most relevant for understanding magnon dynamics. However, since Chern numbers can redistribute between bands via TPTs, contributions from higher-energy bands must also be considered. To capture these effects, we extend our analysis to include higher bands, particularly in Model 1.

In Section 4.1 (Model 1), we compute the Chern numbers for the lowest eight magnon bands and analyze the evolution of band topology under increasing magnetic field. We demonstrate how field-induced TPTs and gap closures generate a rich landscape of topological magnon phases. Of particular importance are the second and third magnon gaps, whose topological character and associated TESs are investigated as a function of the NN DMI (or SkX periodicity w_0).

After establishing the general behavior using Model 1, we focus on the lowest four bands in Models 2 and 3, limiting our analysis to the TESs in the corresponding low-energy gaps. Despite the significant differences in the intrinsic parameters (J , \mathcal{A} , and D), we show that all three models exhibit consistent topological behavior in the low-energy sector, including the field-induced evolution of magnon bands and TESs.

4.1. Model 1: CrI_3 with large magnetic anisotropy

Model 1 features a relatively large magnetic anisotropy \mathcal{A}_1 (see Table 1), which stabilizes skyrmion crystals only when the NN DMI exceeds a threshold value, approximately $d \gtrsim 0.45 J_1$. At this threshold, the skyrmion lattice forms with the largest skyrmion size, $w_0 = 11a$, at minimal magnetic field (where a is the honeycomb lattice constant). As d increases, the skyrmion width and SkX periodicity decrease.

We find that the topological evolution of the second gap with increasing magnetic field is robust across all values of d , owing to the stable nontrivial Chern number of the second band (ED mode). In contrast, the third gap exhibits a periodicity-dependent behavior. Its field evolution is consistent only at high magnetic fields, whereas at low fields, the gap's topological character depends sensitively on whether the initial periodicity exceeds a critical value, identified as $w_0 = 5a$ in Model 1. We demonstrate our results using three representative values of the NN DMI: $d = J_1$, which corresponds to the critical periodicity ($w_0 = 5a$), and $d = 0.7 J_1$ and $d = 0.45 J_1$, which correspond to larger skyrmion widths ($w_0 > 5a$) above the critical periodicity.

4.1.1. SKXs at strong NN DMI ($d = J_1$)

For $d = J_1$, the minimum magnetic field required to stabilize the SkX is approximately $5.5 T$. At this field, the SkX is densely packed, and the Vampire sLLG results are best modeled by skyrmions with width $w_0 = 5a$ (Figure 1a). The corresponding magnetic unit cell contains 50 inequivalent sites (or spins). As the magnetic field B increases, the skyrmions shrink in size and are eventually annihilated beyond approximately $18.25 T$. The skyrmion size as a function of B , determined numerically as described in Section 2, is shown in Figure 1b.

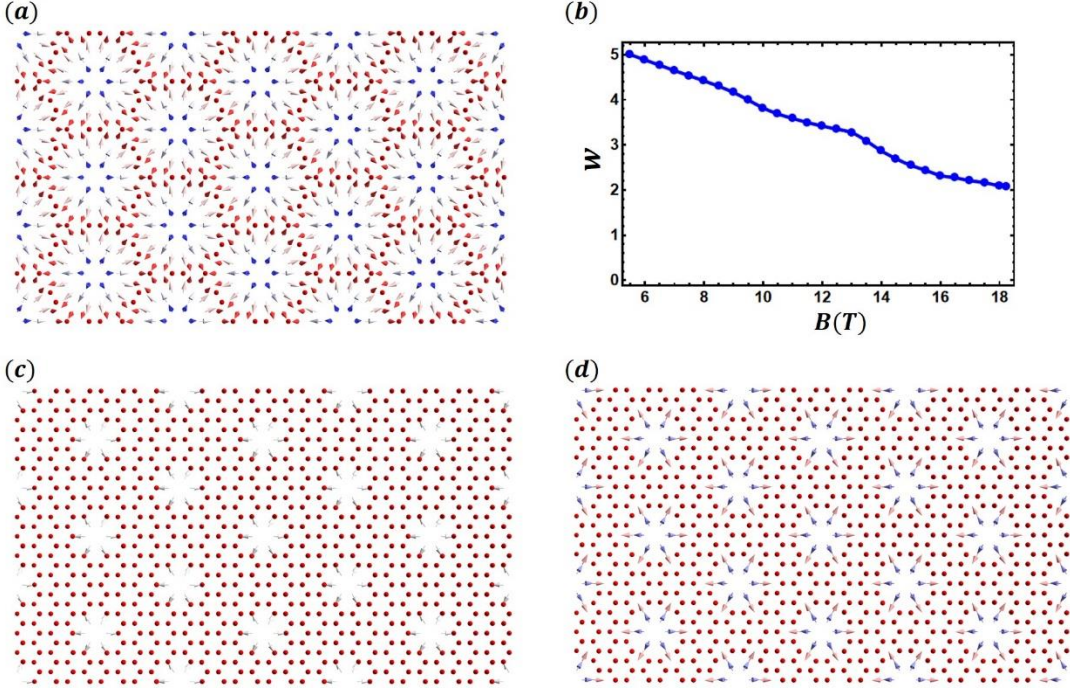


Figure 1: (a) Densely packed SkX at the minimal magnetic field $B_{min} = 5.5$ T for $d = J_1$, modeled with a skyrmion width $w_0 = 5a$ and 50 spins per unit cell. (b) Skyrmion width w as a function of the magnetic field. The dots are computed using Equation 2d with sLLG data, while the solid line is a plot of an interpolation function. (c) Over-shrunk skyrmion configuration at $B = 18.25$ T. (d) SkX at $B = 13.5$ T with $w \approx 3.08 a$, marking the upper bound of the field range used for magnon analysis (5.5 T $\leq B \leq 13.5$ T), chosen to avoid over-shrunk skyrmions.

At high magnetic fields, the skyrmions become very small and resemble localized defects embedded in a nearly uniform ferromagnetic background (Figure 1c). These configurations deviate significantly from the densely packed SkX and are excluded from our magnon analysis. Specifically, for $d = J_1$, we compute the magnon spectrum within the range 5.5 T $\leq B \leq 13.5$ T, ensuring that the skyrmion width remains larger than $3a$. The SkX structure at 13.5 T is shown in Figure 1d.

The lowest nine magnon bands at the minimal field (5.5 T) are shown in Figure 2a, plotted along the high-symmetry directions of the SkX BZ. While our primary focus is on the lowest eight bands in Model 1, the ninth band is included to capture all relevant TPTs and to understand changes in the Chern number of the eighth band. We label the magnon bands by E_n and their associated Chern numbers by C_n , with $n = 1, 2, \dots$ in increasing energy order. The Chern numbers for the lowest eight bands in Figure 2a are $\{C_1, C_2, \dots, C_8\} = \{0, -2, 3, -3, 4, 1, 1, 0\}$, corresponding to the topological phase P_1 .

To understand the nature of the obtained modes, we analyzed the time evolution of the real-space out-of-plane magnetization for bands E_1 through E_5 at the BZ center. The lowest-energy band E_1 is a topologically trivial ($C_1 = 0$) CW rotation mode, similar to what is observed in triangular spin-lattice SkXs. The second band E_2 corresponds to the ED mode. While this mode is topologically trivial in the triangular spin-lattice SkX, it is topological in the honeycomb spin-lattice SkX, with a Chern number $C_2 = -2$.

The third band E_3 is the CCW rotation mode and carries a Chern number $C_3 = 3$, which differs from the triangular $d = J$ case, where the same mode has a Chern number of 1. The fourth band E_4 , identified as the breathing mode, has a Chern number $C_4 = -3$, again in contrast to the triangular case, where this mode carries a Chern number of 1. The fifth band E_5 , associated with the triangular distortion mode, has a Chern number $C_5 = 4$. In the triangular spin-lattice SkX, however, this mode is topologically trivial and lies below the breathing mode at minimal magnetic field and $d = J$.

The NNN DMI is known to induce topological bands in the collinear ferromagnetic phase of honeycomb magnets [23–25,27,51]. One might therefore suspect that the distinct topological features of the honeycomb-based SkX, particularly the nontrivial topology of the second band, arise from the NNN DMI. However, our calculations show that the topological phase P_1 remains unchanged when the NNN DMI is set to zero. This confirms that the nontrivial topology of these bands is not due to the NNN DMI but instead emerges from the chiral spin ordering inherent to the two-sublattice honeycomb structure. This finding highlights the intrinsic capacity of the honeycomb lattice to induce additional magnon band topology that is absent in triangular-based SkXs with the same skyrmion configuration (Néel-type ferromagnetic SkXs).

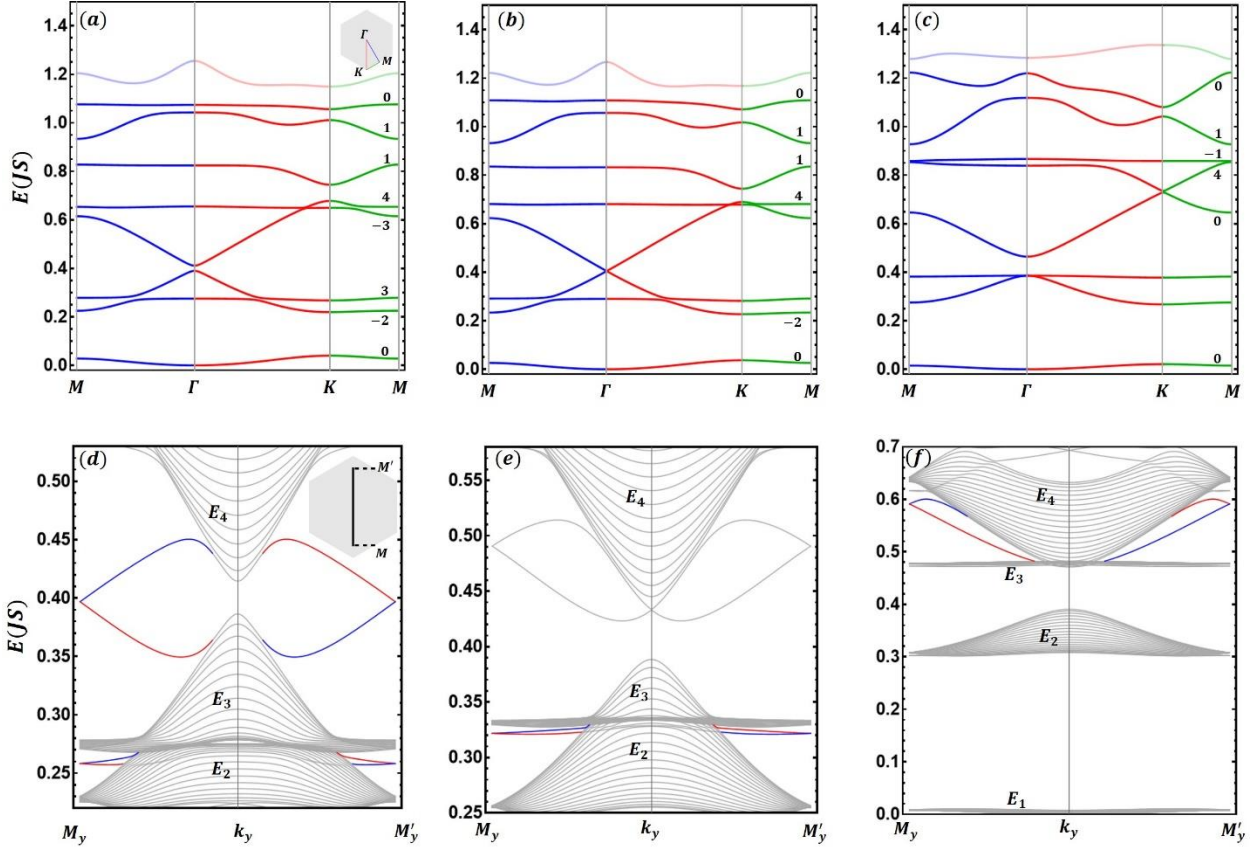


Figure 2: (a) Lowest nine magnon bands at $d = J_1$ and minimal magnetic field 5.5 T. The bands are plotted along the high-symmetry directions of the SkX BZ, as indicated in the inset. Chern numbers for the lowest eight bands are listed. (b) Band structure at $B = 5.91$ T, where the CCW–breathing gap closes, leading to a TPT that trivializes the associated TESs. (c) Band structure at $B = 8.04$ T, where the ED–breathing gap closes, resulting in the trivialization of TESs in that gap. (d–f) TESs computed in a strip geometry at $B = 5.5$ T, 7 T, and 9.45 T, respectively. The spectra are plotted along the $M_yM'_y$ segment of the BZ (solid black line in the inset). TESs are highlighted in red and blue, representing chiral modes propagating in opposite directions along the strip edges. At 5.5 T (d), both the second and third gaps host TESs. At 7 T (e), the third gap becomes topologically trivial following its closure and reopening at 5.91 T, while the second gap remains topological. At 9.45 T (f), the second gap becomes trivial after a TPT at 8.04 T, and TESs reemerge in the third gap.

The nonzero Chern numbers obtained from the magnon band structure indicate the presence of topologically protected magnon edge modes within the bulk band gaps. According to the bulk–edge correspondence, the number of TESs within a given gap equals the total Chern number of all bands below that gap. At the minimal magnetic field $B_{min} = 5.5$ T, both the second gap (between the ED and CCW modes) and the third gap (between the CCW and breathing modes) host chiral TESs, as dictated by $C_1 + C_2 = -2$ and $C_1 + C_2 + C_3 = 1$, respectively. These TESs are illustrated

in Figure 2d, computed using a strip geometry that is infinite along the y -direction and finite along the x -direction. The TESs (highlighted in red and blue) are chiral, propagating unidirectionally along opposite edges of the strip.

Upon increasing the magnetic field above B_{min} , the magnon band structure undergoes a sequence of TPTs, which occur when bulk band gaps close and reopen at critical field values. Specifically, increasing B from $5.5\text{ }T$ to $13.5\text{ }T$ yields 15 TPTs, each associated with a band gap closure as shown in Figure 3 and Supplementary Video SV1. These transitions redistribute Chern numbers among the bands and produce a total of 16 distinct topological magnon phases (see Supplementary Table ST1, Supplementary Video SV1, and Figure 3).

Two particularly interesting TPTs occur at $B \approx 5.91\text{ }T$ (Figure 2b) and $B \approx 8.04\text{ }T$ (Figure 2c). The first field closes the CCW–breathing gap and induces a transition from phase $P_1 = \{0, -2, 3, -3, 4, 1, 1, 0\}$ to $P_2 = \{0, -2, 2, -2, 4, 1, 1, 0\}$. After the gap reopens in phase P_2 , the CCW and breathing modes exchange part of their topological character, yielding $(C_3, C_4) = (2, -2)$. Particularly, one unit of Chern number from each mode is annihilated due to hybridization at the band-touching point. Moreover, the modes undergo an inversion: the second band becomes the breathing mode, while the third band becomes the CCW mode. This TPT also trivializes the edge state in the third gap, since $C_1 + C_2 + C_3 = 0$ in phase P_2 (Figure 2e). However, the edge states in the second gap, now between the ED and breathing modes, remain present.

It is worth noting that a similar TPT, involving band inversion and edge state trivialization in the third gap, has been reported for triangular spin-lattice SkXs at $d = J$ [4]. However, the associated band topology before and after the transition differs from the present case. In the triangular spin-lattice SkX, the Chern numbers for the lowest four bands change from $\{0, 0, 1, 1\}$ to $\{0, 0, 0, 2\}$, indicating a different redistribution of topological charge.

At the higher field $B \approx 8.04\text{ }T$, the ED–breathing gap (i.e., the second gap) closes and inverts the corresponding modes. After reopening, the second band corresponds to the breathing mode, while the third band becomes flatter and corresponds to the ED mode (see Supplementary Video SV1 and Supplementary Figure S3a). This is accompanied by a transition from phase $P_6 = \{0, -2, 2, 0, 4, -1, 1, 0\}$ to $P_7 = \{0, 0, 0, 0, 4, -1, 1, 0\}$, in which $C_2 = C_3 = 0$. Both bands become topologically trivial after the transition, effectively eliminating the TESs from the second gap (Supplementary Figure S3a).

Beyond $8.04 T$, C_2 remains zero up to the maximal field of $13.5 T$ (see Supplementary Table ST1), indicating that the second gap no longer hosts TESs. In contrast, the third band reacquires a nonzero Chern number ($C_3 = 3$) in the field range $9.36 T < B \leq 13.5 T$, where the third gap lies between the ED and CCW modes. This reactivation of TESs at relatively high magnetic fields is illustrated in Figure 2f.

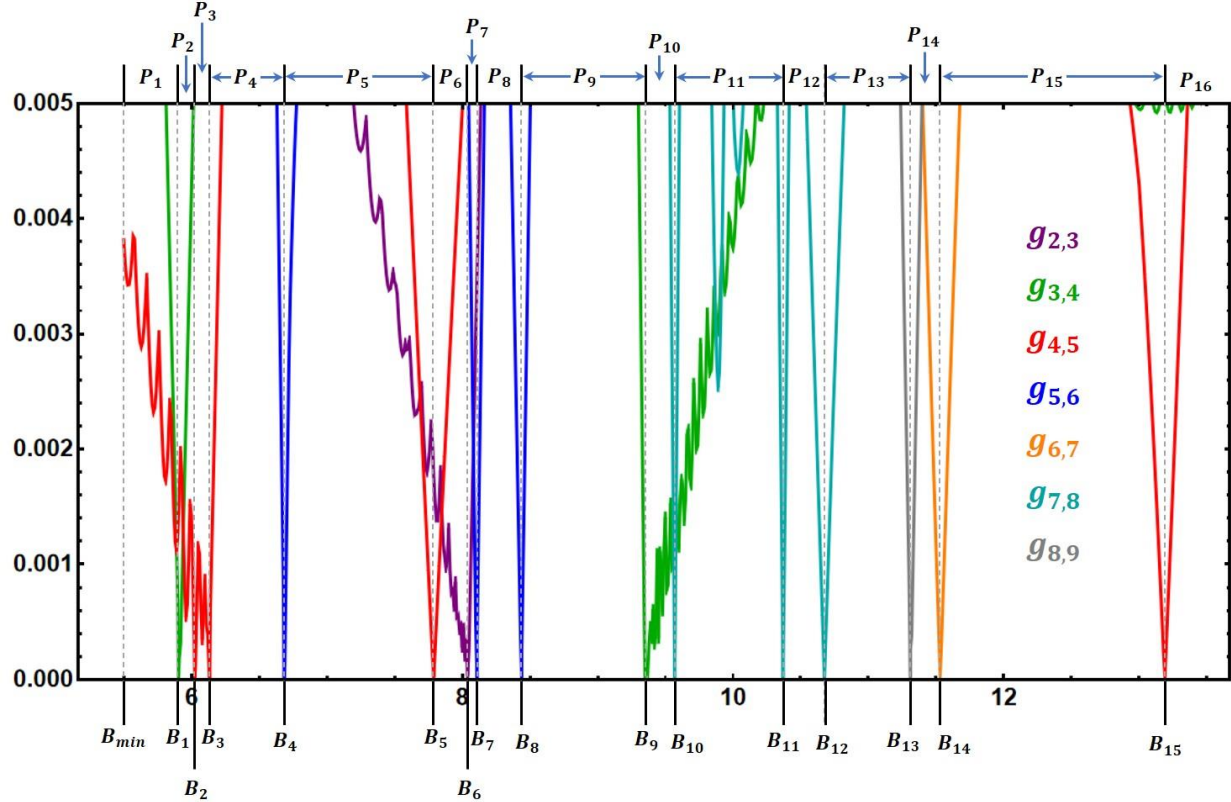


Figure 3: Minimal values of the energy gaps $g_{i,i+1}$ between adjacent magnon bands E_i and E_{i+1} as a function of the magnetic field for $d = J_1$ (Model 1), expressed in units of $J_1 S$. The corresponding critical magnetic field values B_1, \dots, B_{15} , at which these gaps close and trigger TPTs, are listed in Supplementary Table ST1. The Chern numbers for the resulting topological phases P_1, \dots, P_{16} are also provided therein.

We have seen that at $d = J_1$ and $w_0 = 5 a$, both the second and third gaps are topological at low magnetic fields. The TESs in the third gap resemble those found in triangular-lattice SkXs at $d = J$, whereas the TESs in the second gap are distinctive to the honeycomb spin-lattice and have no counterpart in the triangular case. Upon increasing the field, hybridization between the CCW and breathing modes causes the third gap to close and reopen, thereby trivializing the associated TESs.

In the coming sections (4.1.2 and 4.1.3), we show that for $w_0 > 5 a$ the third gap is topologically trivial at minimal field and TESs in this gap can only emerge at higher fields.

In contrast, the second gap exhibits consistent behavior across different values of w_0 . It is topological at low magnetic fields and becomes trivial beyond a critical field. Although these claims could also be demonstrated for $w_0 = 6 a$, we defer to larger values of w_0 in the subsequent sections to ensure clearer figures and a more evident illustration of how increasing w_0 enriches the magnon topological phase diagram.

4.1.2. SKXs at a weaker NN DMI ($d = 0.7 J_1$)

At $d = 0.7 J_1$, the densely packed CrI_3 SkX emerges at $B_{min} \approx 2.8 T$, with $w_0 = 7 a$ (Figure 4a) and 98 spins per skyrmion. The variation of skyrmion size with magnetic field is shown in Figure 4b. The SkX remains stable up to approximately $9.2 T$ (Figure 4c). As in the $d = J_1$ case, we avoid over-shrunk skyrmions and focus our magnon analysis on the range $2.8 T \leq B \leq 8.4 T$. The SkX at $8.4 T$, with skyrmion width $w \approx 3a$ and inter-skyrmion spacing of $7a$, is depicted in Figure 4d. The low-energy magnonic bands at the minimal magnetic field ($2.8 T$) are shown in Figure 5a. The system at this point resides in topological phase $P_{17} = \{0, -2, 2, -2, 4, 1, -1, 2\}$, which differs from the 16 phases observed previously at $d = J_1$. However, the Chern numbers for the lowest six bands in P_{17} match those in phase $P_2 = \{0, -2, 2, -2, 4, 1, 1, 0\}$, which was realized at $d = J_1$ following the closure of the third gap. Moreover, the modal character of bands E_1 through E_5 in P_{17} is consistent with that of P_2 ; these correspond to the CW, ED, breathing, CCW, and triangular distortion modes, respectively. As in P_2 , the third gap in P_{17} is topologically trivial (TESs are absent), while the second gap hosts TESs driven by $C_2 = -2$ (Figure 5c). The triviality of the third gap at minimal magnetic field marks a fundamental difference from the $d = J_1$ case and from previous results on triangular-based SkXs, where this gap is predicted to be generically topological.

As the magnetic field increases from $2.8 T$ to $8.4 T$, the system undergoes 24 TPTs, as a result of the band gap closures shown in Figure 6 (see also Supplementary Video SV2 and Supplementary Table ST2). These transitions give rise to 25 distinct topological phases, among which 21 are new, while four phases (P_6, P_8, P_9 , and P_{12}) were already encountered in the $d = J_1$ case. Notably, the CCW and breathing modes do not hybridize at any field value when $d = 0.7 J_1$ (Figure 6 and Supplementary Video SV2).

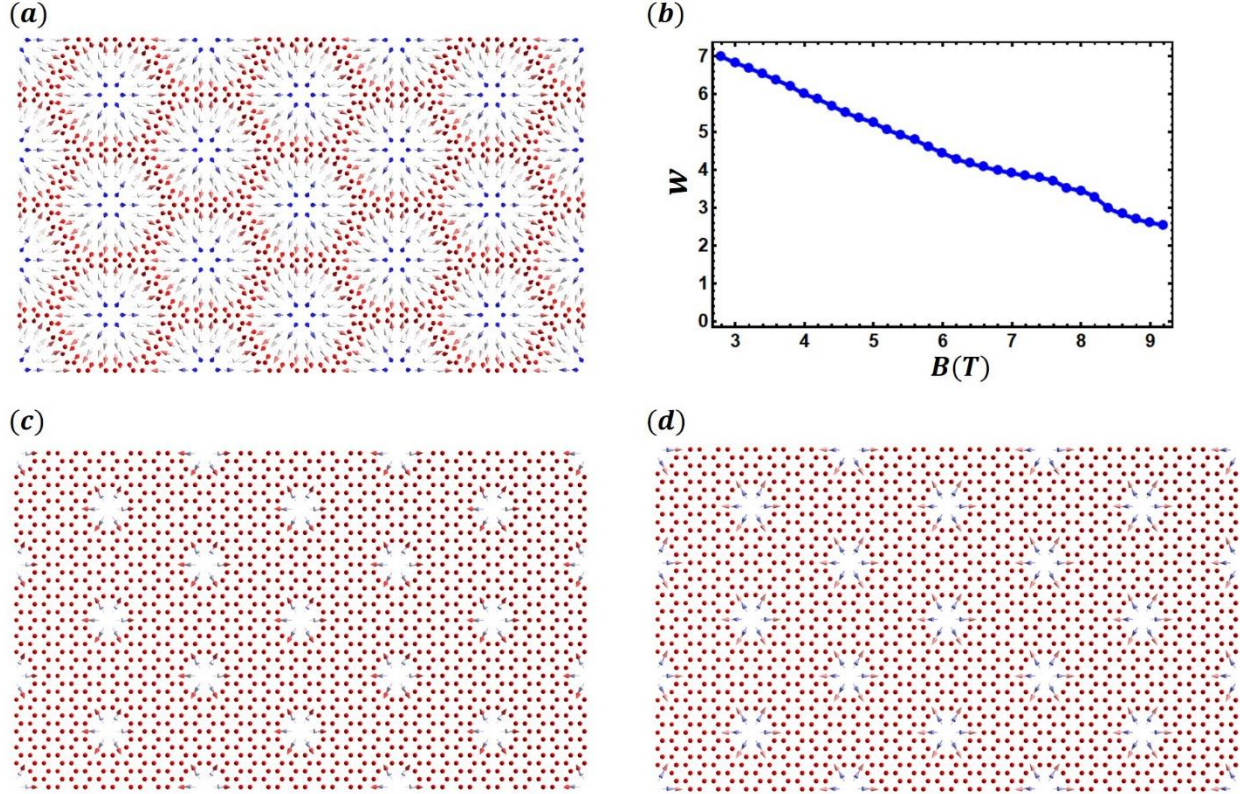


Figure 4: (a) The densely packed SkX at $d = 0.7 J_1$ and minimal magnetic field $2.8 T$, with skyrmion width $w_0 = 7a$ and 98 spins per skyrmion. (b) The skyrmion width w as a function of the magnetic field, computed from the field-dependent out-of-plane spin density using the method described in Section 2. (c) The SkX at $B = 9.2 T$, where skyrmions shrink significantly. (d) The SkX at $B = 8.4 T$ used as the upper bound in the magnon analysis to avoid over-shrunk skyrmions.

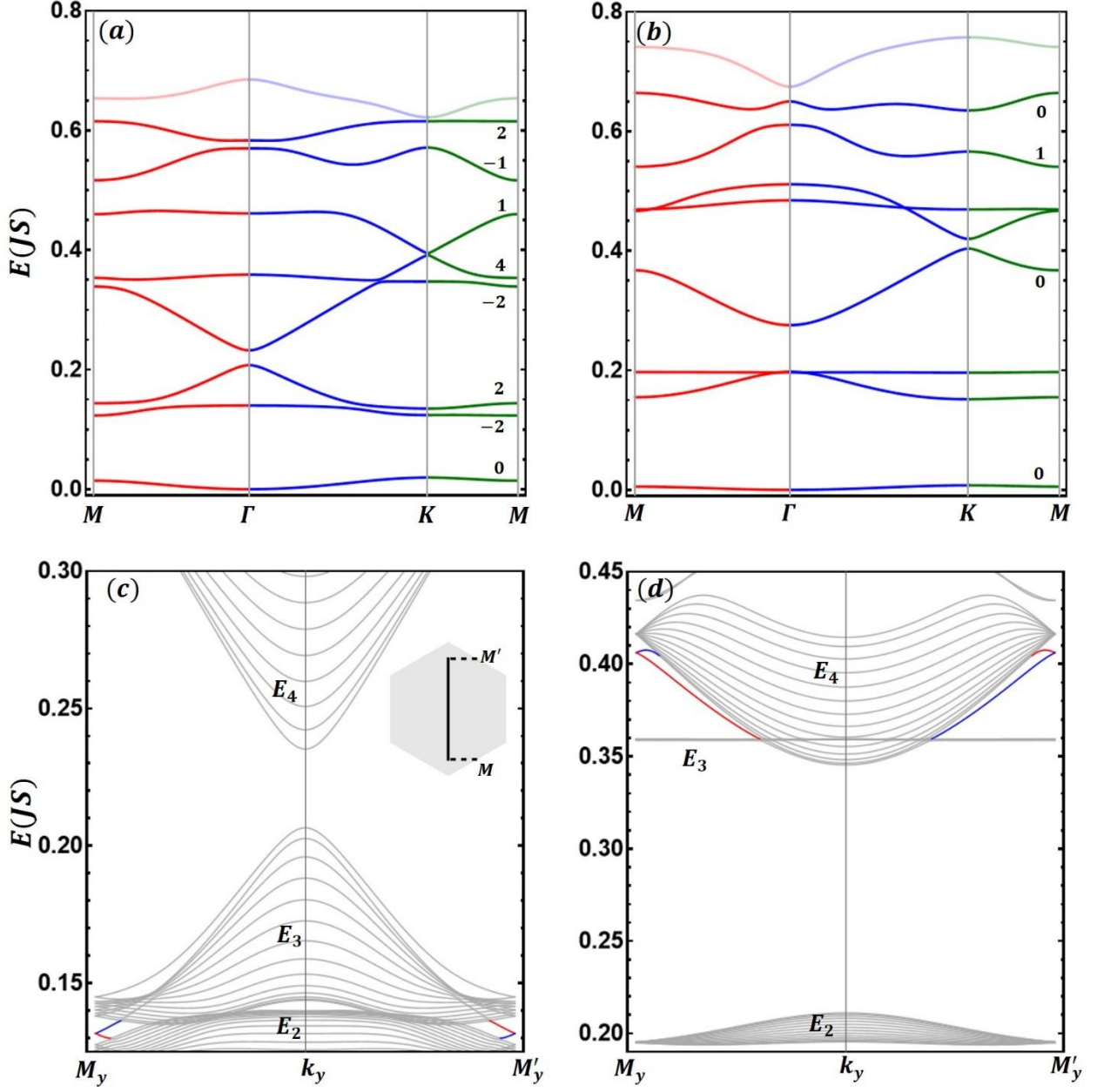


Figure 5: (a) Lowest nine magnon bands at $d = 0.7J_1$ and minimal magnetic field $B = 2.8\text{ T}$, corresponding to topological phase $P_{17} = \{0, -2, 2, -2, 4, 1, -1, 2\}$. (b) Band structure at $B = 3.91\text{ T}$, where the ED-breathing gap (second gap) and the fifth gap close simultaneously, inducing a TPT that trivializes the TESs in the second gap. (c, d) TESs (red and blue) computed in a strip geometry shown for $B = 2.8\text{ T}$ and 5.66 T , respectively. TESs are present in the second gap at 2.8 T (c), and in the third gap at 5.66 T (d).

The magnetic field evolution of the Chern numbers (Supplementary Video SV2 and Supplementary Table ST2) shows that the second gap hosts TESs only within the field range $2.8\text{ T} \leq B < 3.91\text{ T}$. TESs in this gap at 2.8 T are shown in Figure 5c. The second gap closes

simultaneously with the fifth gap at the critical field $B \approx 3.91 T$ (Figure 5b, Figure 6, and Supplementary Video SV2), resulting in a TPT from $P_6 = \{0, -2, 2, 0, 4, -1, 1, 0\}$ to $P_8 = \{0, 0, 0, 0, 1, 2, 1, 0\}$, which trivializes the second gap (Supplementary Figure S3b). In contrast, the third gap becomes topological only in the high-field range $5.5 T < B < 6.08 T$ and is otherwise trivial. In this range, as in the $d = J_1$ case, the third gap separates the ED and CCW modes (Supplementary Video SV2), carrying Chern numbers 3 and -3 , respectively. TESs are supported in the third gap over this field range (Figure 5d), driven by $C_1 + C_2 + C_3 = 3$.

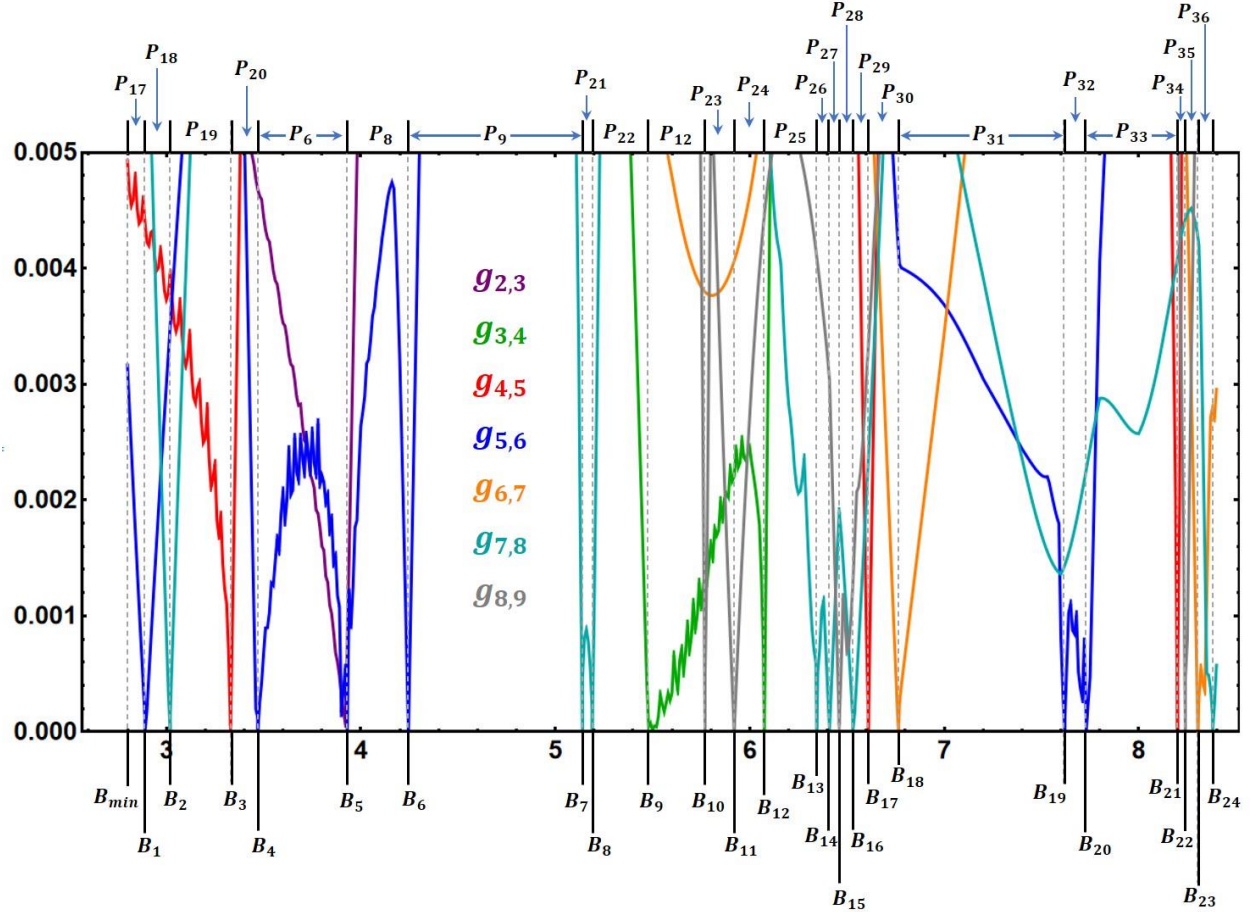


Figure 6: Minimal values of the energy gaps $g_{i,i+1}$ between adjacent magnon bands E_i and E_{i+1} as a function of the magnetic field for $d = 0.7 J_1$ (Model 1), expressed in units of $J_1 S$. The critical magnetic field values B_1, \dots, B_{24} , and the Chern numbers for the topological phases P_{17}, \dots, P_{37} are listed in Supplementary Table ST2.

The $d = 0.7 J_1$ case illustrates how magnetic fields can create and annihilate TESs in the second and third gaps over non-overlapping field intervals. Furthermore, these results demonstrate that

the topological field-induced behavior of the third gap is not universal across different NN DMI values. In contrast, the second gap shows consistent behavior between the $d = J_1$ ($w_0 = 5a$) and $d = 0.7 J_1$ ($w_0 = 7a$) cases. To further examine these trends, we next consider the threshold NN DMI value ($d = 0.45 J_1$) required to stabilize SkXs in Model 1 of CrI_3 .

4.1.3. SKXs at threshold NN DMI ($d = 0.45 J_1$)

At the threshold value of the NN DMI, $d = 0.45 J_1$, a densely packed SkX emerges at $B_{min} \approx 0.8 T$, characterized by a skyrmion width $w_0 = 11 a$ (Figure 7a) and 242 spins per skyrmion. The SkX phase remains stable within the magnetic field range $0.8 T \leq B \leq 3.2 T$ (Figure 7b), during which the skyrmions retain a substantial size, with $4.27 a$ at the upper field bound. Accordingly, we analyze the magnon spectrum over the full stability range of the SkX phase.

The low-energy magnon bands at $d = 0.45 J_1$ and $B = 0.8 T$ correspond to a new topological phase, $P_{38} = \{0, -2, 2, -2, 2, 3, -3, 4\}$, shown in Figure 7c. This phase shares the same Chern numbers and modal character in the lowest four bands as the $d = 0.7 J_1$ case. Consequently, at minimal field, the breathing–CCW (third) gap is topologically trivial, while the ED–breathing (second) gap hosts TESs, as illustrated in Figure 7d.

Upon increasing the magnetic field, the system undergoes 30 TPTs driven by band gap closures (Figure 8, Supplementary Video SV3, and Table ST3), resulting in 28 new topological phases in addition to P_{18} , which was previously encountered at $d = 0.7 J_1$. As in that case, the breathing and CCW modes remain spectrally separated throughout the full field range.

The second gap supports TESs exclusively within the low-field range $0.8 T \leq B < 0.97 T$. At $B \approx 0.97 T$, the simultaneous closure of the second and eighth gaps induces a TPT from $P_{40} = \{0, -2, 2, 0, 0, 3, -1, -4\}$ to $P_{41} = \{0, 0, 0, 0, 0, 3, -1, 2\}$, thus trivializing the second gap (Supplementary Figure S3c).

While the third gap lacks a consistent topological behavior at low magnetic fields across different values of w_0 , we find that it becomes topological at sufficiently high magnetic fields for any w_0 . In the current case, the third gap is topological within the range $1.96 T < B < 2.09 T$, where it separates the ED and CCW modes, with $C_1 + C_2 + C_3 = 3$ (see Supplementary Table ST3).

The analysis in Section 4.1 thus establishes a robust trend: the second gap consistently hosts TESs at low fields and becomes trivial beyond a critical field, regardless of w_0 . In contrast, the third gap is topological at higher fields, with its behavior at low fields depending sensitively on the SkX

periodicity. In particular, the third gap is topological at low fields only when $w_0 \leq 5a$ for Model 1. In the following sections, we investigate the robustness of these findings to variations in the intrinsic magnetic parameters, specifically the NNN DMI D and the SIMA \mathcal{A} , by analyzing Models 2 and 3. We show that while D has negligible influence on the qualitative behavior, \mathcal{A} shifts the critical w_0 , which increases as \mathcal{A} decreases.

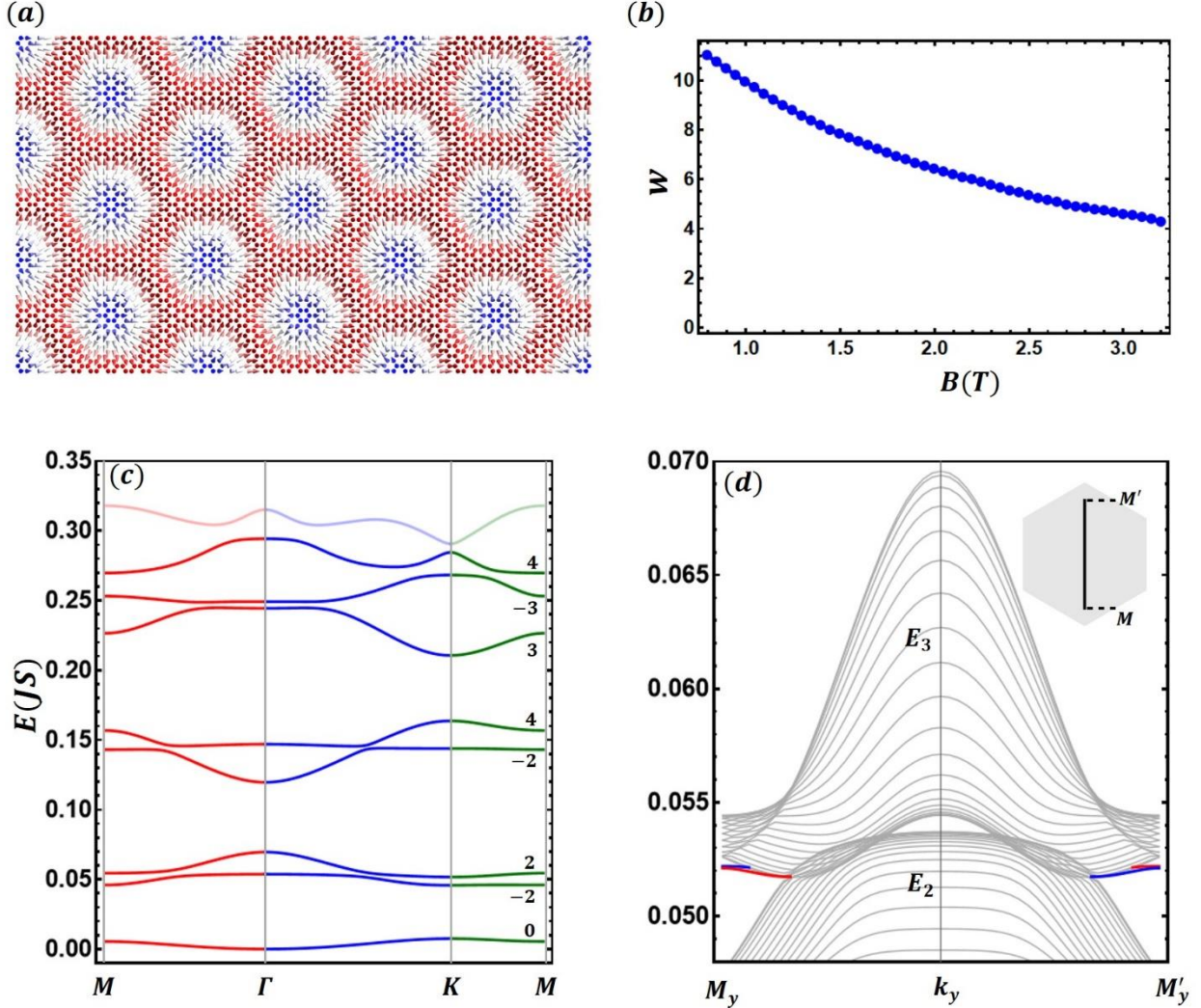


Figure 7: (a) Densely packed SkX configuration at $d = 0.45 J_1$ and minimal magnetic field $B = 0.8 T$, characterized by a skyrmion width $w_0 = 11 a$. (b) Magnetic-field dependence of the skyrmion width w . (c) The lowest nine magnon bands at $d = 0.45 J_1$ and minimal field $B = 0.8 T$, corresponding to the SkX phase in (a) and associated with topological phase $P_{38} = \{0, -2, 2, -2, 2, 3, -3, 4\}$. (d) Chiral TESs (red and blue curves) in the second gap at $B = 0.8 T$ computed in a strip geometry. The third gap does not support TESs in this case.

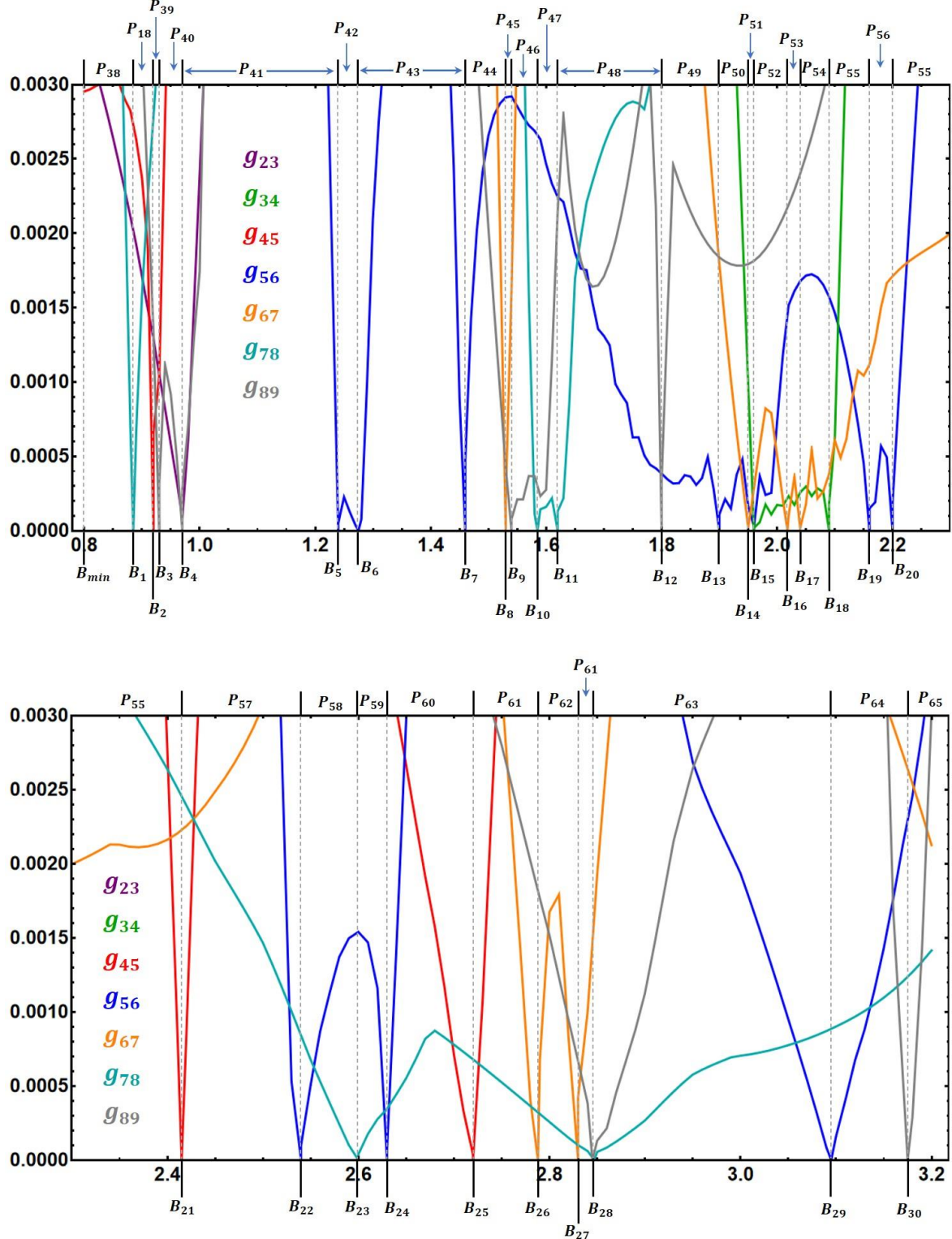


Figure 8: Minimal values of the energy gaps $g_{i,i+1}$ between adjacent magnon bands E_i and E_{i+1} as a function of the magnetic field for $d = 0.45 J_1$ (Model 1), expressed in units of $J_1 S$. The plot over the magnetic field range $0.8 T \leq B \leq 3.2 T$ is separated into two figures for better clarity. The critical magnetic field values and the Chern numbers for the topological phases are listed in Supplementary Table ST3.

4.2. Model 2: CrI_3 with reduced magnetic anisotropy \mathcal{A}

Model 2 represents an alternative experimental parameterization for CrI_3 , with magnetic parameters listed in Table 1. Both Models 1 and 2 capture the experimentally measured magnon spectrum in the collinear FM phase of CrI_3 . In Model 2, the normalized anisotropy is significantly lower ($\mathcal{A}_2/J_2 \approx 0.058$) than in Model 1 ($\mathcal{A}_1/J_1 \approx 0.103$). This reduction leads to a lower threshold NN DMI required to stabilize SkXs: $d \approx 0.35 J_2 \approx 0.74 \text{ meV}$ with $w_0 = 14a$, compared to $d \approx 0.45 J_1 \approx 0.96 \text{ meV}$ with $w_0 = 11a$ in Model 1. Moreover, the critical SkX periodicity, defined as the threshold below which the third gap becomes topological at low magnetic fields, increases from $5a$ in Model 1 to $6a$ in Model 2 due to the lower magnetic anisotropy. To test the robustness of conclusions drawn from Model 1, we consider representative SkXs in Model 2 with $w_0 = 6a$ ($d = 0.85 J_2$) and $w_0 = 14a$ ($d = 0.35 J_2$).

For $w_0 = 6a$ at $d = 0.85 J_2$, the SkX forms at approximately 4.4 T . We examine the magnon spectrum within the range $4.4 \text{ T} \leq B \leq 11.9 \text{ T}$, where the skyrmion width reduces to $w \approx 3.1a$ at 11.9 T . The lowest nine magnon bands at 4.4 T are shown in Figure 9b, with the four lowest modes (E_1, \dots, E_4) corresponding to the CW, ED, CCW, and breathing modes. The evolution of the spectrum under increasing magnetic field results in eight distinct topological phases, captured in Supplementary Video SV4 and Figure 9a. We compute the Chern numbers for the lowest four bands, which are sufficient to characterize TESs in the second and third gaps. The second gap is topological in the range $4.4 \text{ T} \leq B < 6.85 \text{ T}$ and becomes trivial beyond that. The third gap is topological in the low-field interval $4.4 \text{ T} \leq B < 4.89 \text{ T}$ and again in the high-field interval $8.48 \text{ T} < B < 10.14 \text{ T}$, separating the ED and CCW modes with Chern numbers $+3$ and -3 . Examples of TESs in the second and third gaps, particularly at 4.4 T , are shown in Figure 9c. These results are fully consistent with Model 1 for SkXs below (or equal to) the critical periodicity. Next, we analyze the threshold NN DMI $d \approx 0.35 J_2$. SkXs are stabilized within $0.55 \text{ T} \leq B \leq 2.4 \text{ T}$, with $w_0 = 14a$ at 0.55 T and $w \approx 4.49a$ at 2.4 T . The lowest nine bands at 0.55 T are shown in Figure 10b. The four lowest bands correspond to the CW, ED, breathing, and CCW modes (in increasing energy). Across the full magnetic field range, seven distinct topological phases emerge for these bands, captured in Supplementary Video SV4 and Figure 10a. The third gap becomes topological only within the high-field window $1.29 \text{ T} < B < 1.37 \text{ T}$, separating the ED and CCW modes with Chern numbers $+3$ and -3 (Figure 10a and Supplementary Video SV4). Meanwhile, the second gap is topological only at low fields ($0.55 \text{ T} \leq B < 0.655 \text{ T}$),

with TESs illustrated in Figure 10c. Once again, these results align with the findings of Model 1 for SkXs whose periodicity exceeds the critical value.

Before proceeding to Model 3, we emphasize some key observations. First, the critical SkX periodicity below which the third gap is topological at low fields increases with decreasing \mathcal{A} : it shifts from $5a$ in Model 1 to $6a$ in Model 2. Second, the differing values of the NNN DMI D in Models 1 and 2 have a negligible impact on magnon topology, confirming that D does not play a significant role in determining the topological properties of honeycomb-based FM SkXs. Lastly, although only the lowest four bands were analyzed in Model 2, Supplementary Video SV4 reveals a rich set of TPTs involving higher bands, akin to Model 1. However, to maintain brevity, we limit our discussion to the low-energy spectrum in Model 2 (and Model 3).

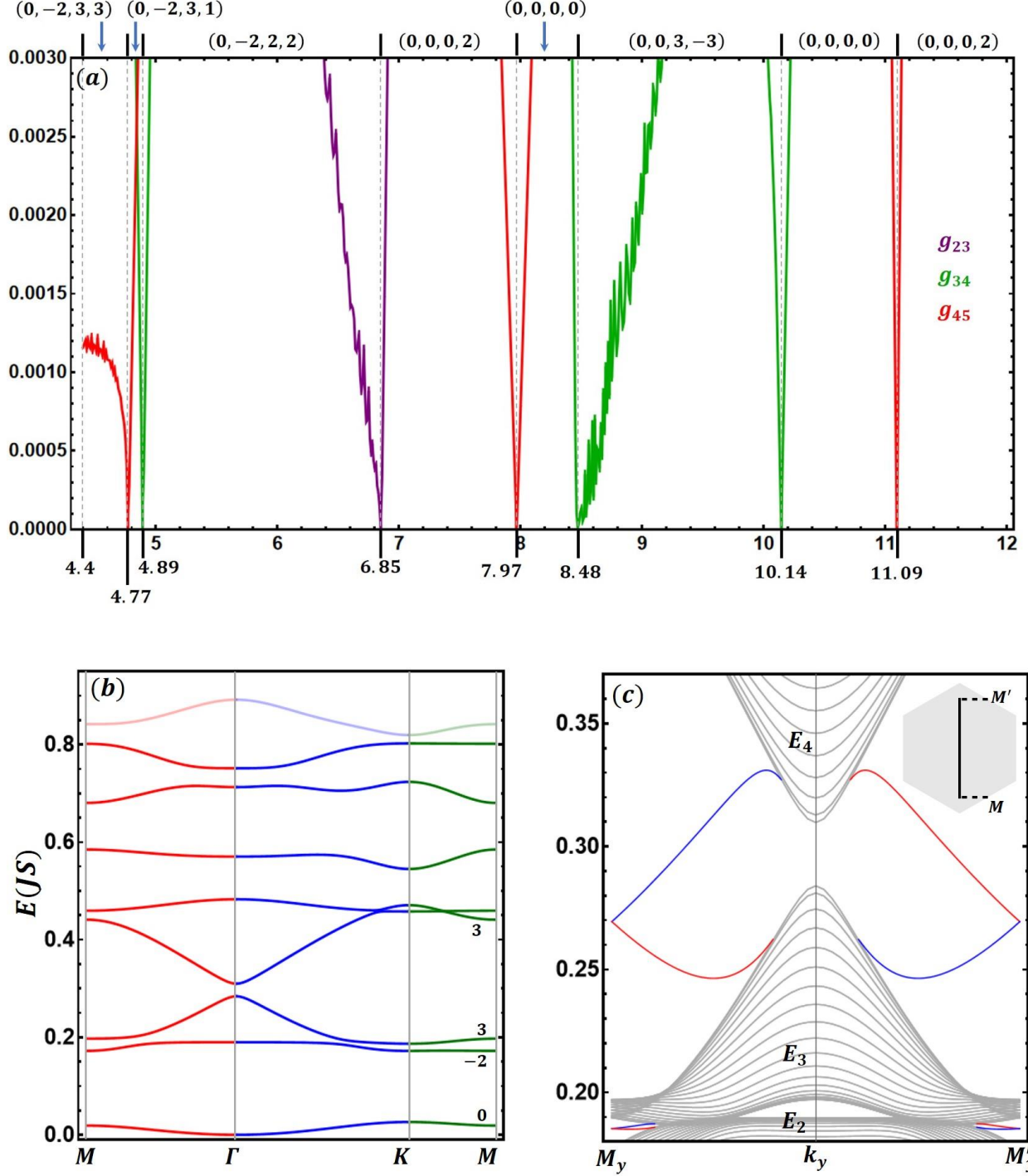


Figure 9: (a) Minimal values of the energy gaps between the lowest four magnon bands plotted as a function of the magnetic field for $d = 0.85 J_2$ (Model 2), expressed in units of J_2S . The critical magnetic fields (in T) defining the boundaries of each topological phase, along with the corresponding Chern numbers, are indicated on the plot. (b) The lowest nine magnon bands at $d = 0.85 J_2$ and minimal field $B = 4.4 T$. The Chern numbers for the lowest four bands are shown. (c) TESs in the second and third magnon gaps (red and blue), computed in a strip geometry at $B = 4.4 T$.

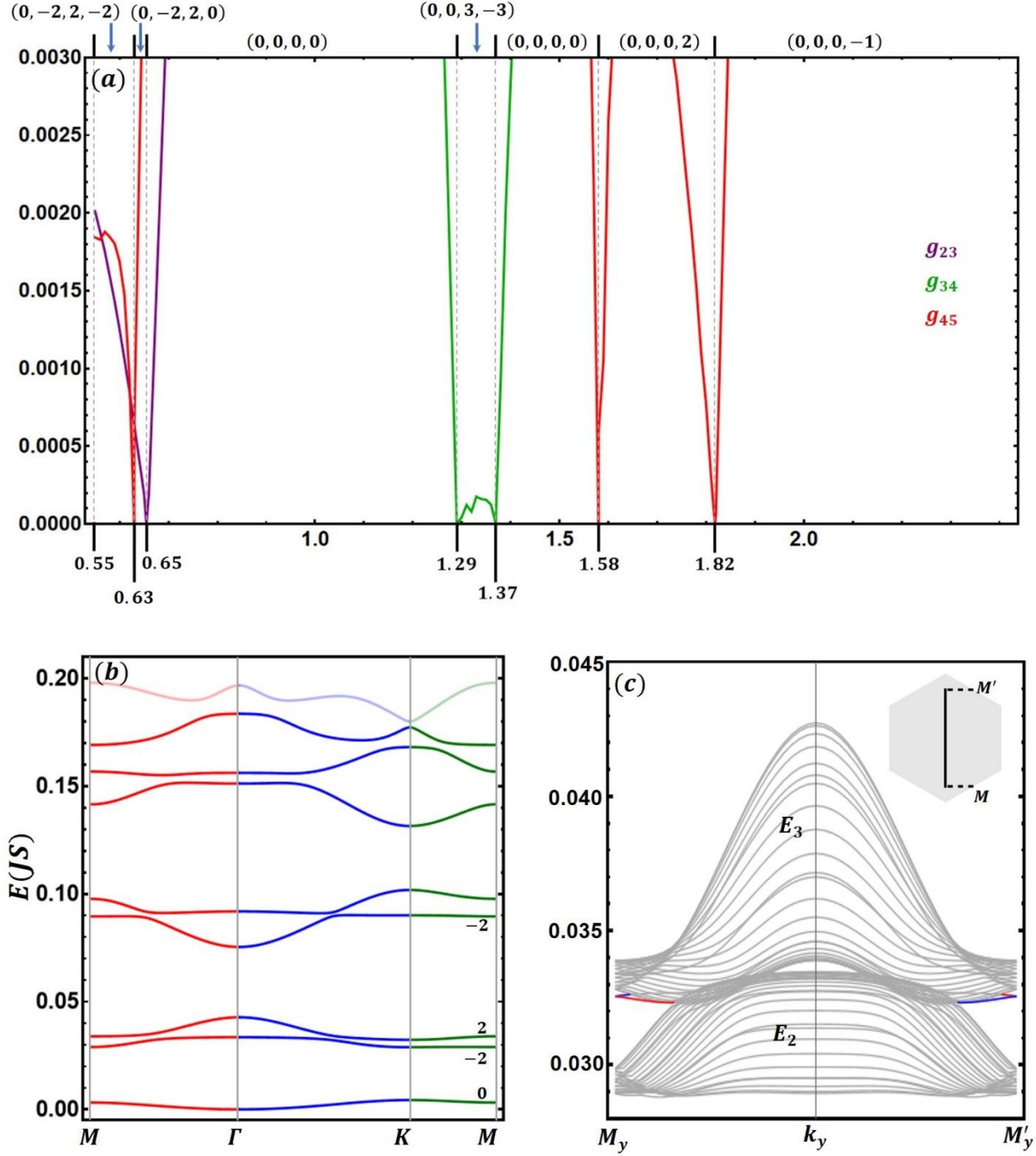


Figure 10: (a) Minimal values of the energy gaps between the lowest four magnon bands plotted as a function of the magnetic field for $d = 0.35 J_2$ (Model 2), expressed in units of J_2S . The critical magnetic fields (in T) defining the boundaries of each topological phase, along with the corresponding Chern numbers, are indicated on the plot. (b) The lowest nine magnon bands at $d = 0.35 J_2$ and minimal field $B = 0.55 T$. The Chern numbers for the lowest four bands are shown. (c) TESs in the second (red and blue), computed in a strip geometry at $B = 0.55 T$. TESs are absent from the third gap (not shown).

4.3. Model 3: $CrBr_3$ with tiny magnetic anisotropy \mathcal{A}

Model 3 accurately describes the experimental magnon dispersion in monolayer $CrBr_3$ in its collinear FM phase. Our interest in this model is multi-fold. First, Model 3 (Table 1) features a very weak SIMA, with $\mathcal{A}_3/J_3 \approx 0.019$, significantly lower than in Models 1 and 2. As a result, the threshold NN DMI required to stabilize SkXs is reduced to $d \approx 0.25 J_3 \approx 0.37 \text{ meV}$, compared to 0.96 meV and 0.74 meV in Models 1 and 2, respectively. This suggests that SkXs may be more readily realizable in $CrBr_3$ than in CrI_3 . Second, the NNN DMI is negligible in this model ($D_3 = 0$), making Model 3 ideal for isolating the effects of weak \mathcal{A} and vanishing D on magnon topology. It thus offers a stringent test of the generality of the conclusions drawn in previous sections.

The critical SkX periodicity in Model 3 is found to be $11a$, larger than the values obtained for Models 1 ($5a$) and 2 ($6a$), reflecting the much smaller anisotropy. To test the robustness of our conclusions, we examine two representative cases: (i) $d = 0.4 J_3$ with $w_0 = 11a$, and (ii) the threshold $d = 0.25 J_3$ with $w_0 = 17a$. For $d = 0.4 J_3$, the SkX phase emerges in the field range $0.8 T \leq B \leq 2.85 T$, with a skyrmion width $w_0 = 11a$ at $B = 0.8 T$ and $w = 3.93a$ at $B = 2.85 T$. The lowest nine energy bands at $B = 0.8 T$ are shown in Figure 11b. Varying the field produces six distinct topological phases for the lowest four bands, presented in Supplementary Video SV5 and Figure 11a. The second and third gaps are topological at low fields in the ranges $0.8 T \leq B < 1.05 T$ and $0.8 T \leq B < 0.865 T$, respectively. Figure 11c presents an example of the TESs in these gaps at $0.8 T$. The second gap becomes trivial for $B > 1.05 T$, while the third gap becomes topological again in the high-field range $1.22 T < B < 1.6 T$ (Supplementary Video SV5 and Figure 11a). For the threshold DMI $d = 0.25 J_3$, the SkX phase is stable in the field interval $0.275 T \leq B \leq 1.225 T$, with $w_0 = 17a$ and $w = 4.9a$ at the minimal and maximal fields, respectively. The band structure at $B = 0.275 T$ is shown in Figure 12b. Field variation generates six topological phases for the lowest four bands, as seen in Figure 12a and Supplementary Video SV5. The third gap is topological only in the range $0.465 < B < 0.555$, whereas the second gap is topological only at low fields, specifically for $0.275 T \leq B < 0.32 T$. Figure 12c presents an example of the TESs in the second gap, specifically at the minimal field $B = 0.275 T$. These findings confirm the consistency of our conclusions across all three models. Despite variations in \mathcal{A} and D , the observed topological behavior of the second and third gaps in honeycomb-based SkXs remains robust.

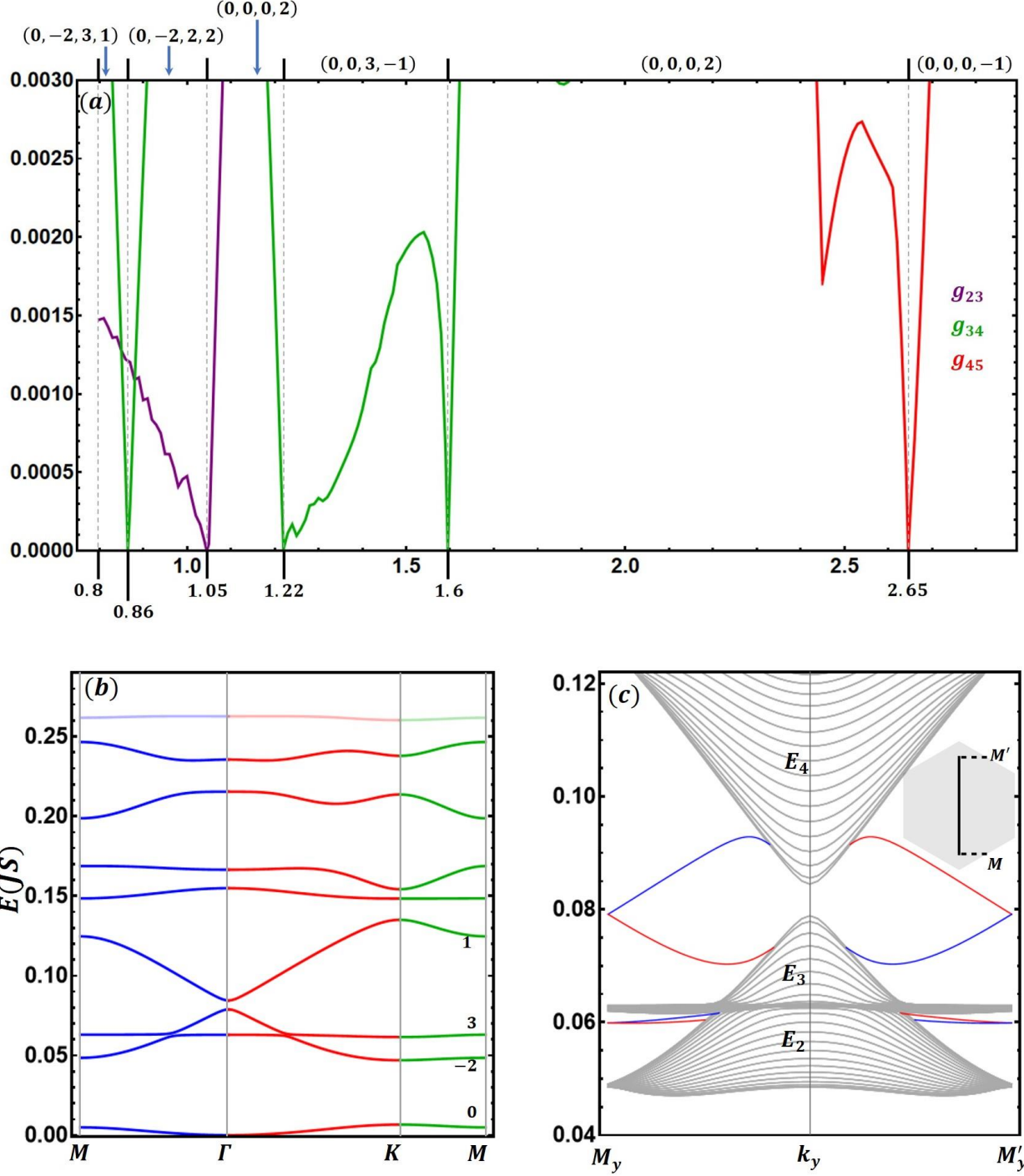


Figure 11: (a) Minimal values of the energy gaps between the lowest four magnon bands plotted as a function of the magnetic field for $d = 0.4 J_3$ (Model 3), expressed in units of $J_3 S$. The critical magnetic fields (in T) defining the boundaries of each topological phase, along with the corresponding Chern numbers, are indicated on the plot. (b) The lowest nine magnon bands at $d = 0.4 J_3$ and minimal field $B = 0.8 T$. The Chern numbers for the lowest four bands are shown. (c) TESs in the second and third gaps (red and blue), computed in a strip geometry at $B = 0.8 T$.

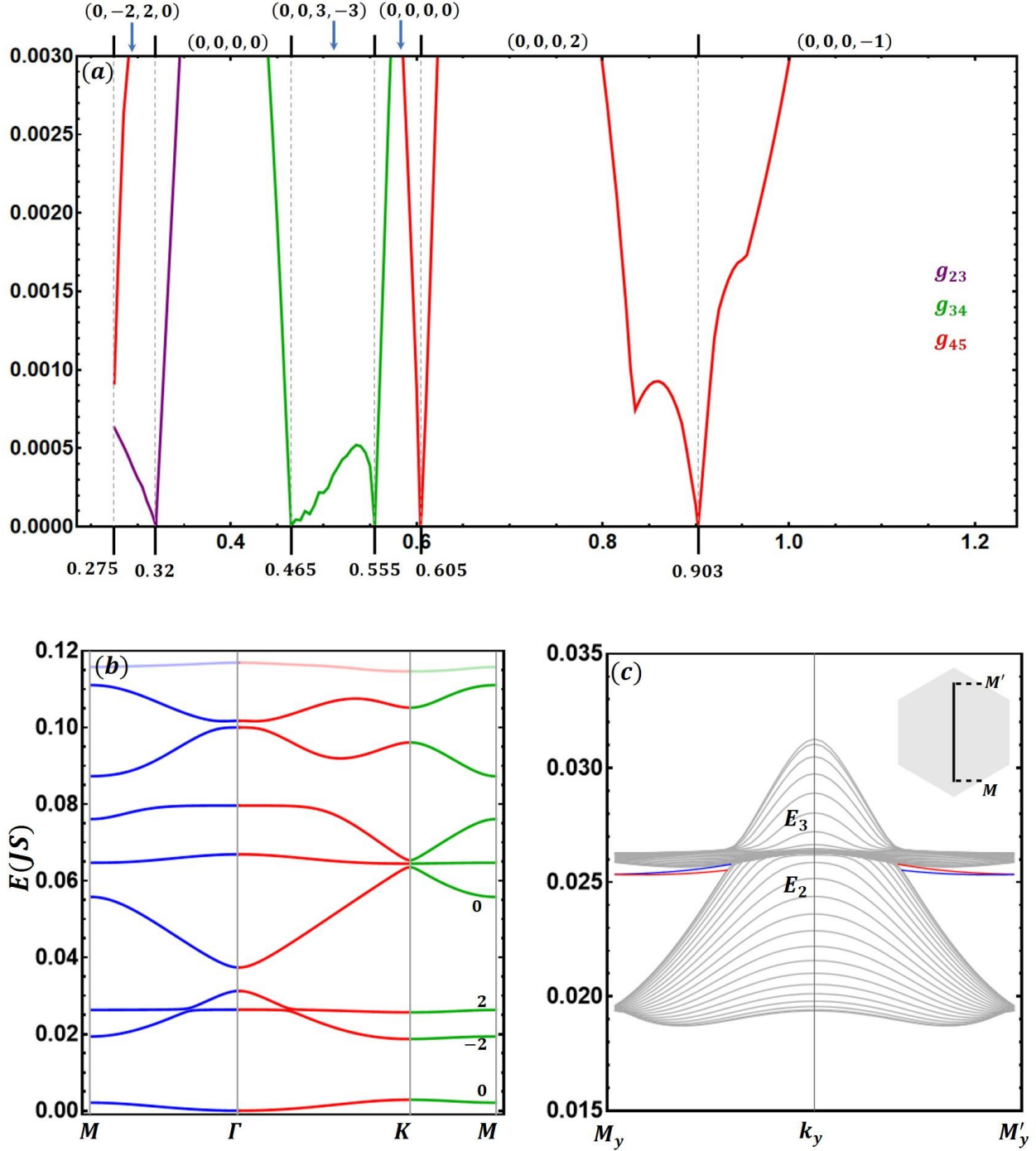


Figure 12: (a) Minimal values of the energy gaps between the lowest four magnon bands plotted as a function of the magnetic field for $d = 0.25 J_3$ (Model 3), expressed in units of $J_3 S$. The critical magnetic fields (in T) defining the boundaries of each topological phase, along with the corresponding Chern numbers, are indicated on the plot. (b) The lowest nine magnon bands at $d = 0.25 J_3$ and minimal field $B = 0.275 T$. The Chern numbers for the lowest four bands are shown. (c) TESs in the second gap (red and blue), computed in a strip geometry at $B = 0.275 T$. TESs are absent from the third gap (not shown).

5. Conclusion

In conclusion, we have theoretically investigated magnon band topology and TESs in Néel-type FM SkXs stabilized on 2D honeycomb spin-lattices. Employing realistic material-specific parameters for monolayers of CrI_3 and $CrBr_3$, our analysis demonstrates that the honeycomb lattice profoundly influences the magnon band topology compared to previously studied Bravais spin-lattices.

Certain characteristic magnon modes, which are topologically trivial in triangular-based SkXs, acquire nontrivial Chern numbers in honeycomb-based systems. The second magnon gap consistently hosts TESs at low magnetic fields, a feature robust against variations in intrinsic magnetic parameters and SkX periodicity. These TESs can be trivialized beyond a critical magnetic field through field-induced topological phase transitions. In contrast, the third magnon gap shows more complex behavior: at low magnetic fields, it is topological only when the SkX periodicity falls below a critical value set by the SIMA \mathcal{A} . Nevertheless, at sufficiently high magnetic fields, the third gap universally becomes topological across all models studied, independent of intrinsic parameters and SkX periodicity.

The comparative analysis of three experimental models indicates that the intrinsic NNN DMI has negligible influence on the magnon topology of honeycomb-based SkXs. Additionally, the results underscore the rich variety and field-induced tunability of topological magnon phases. The simultaneous existence of multiple topological gaps that can be independently switched by external magnetic fields points to potential magnonic multiplexing capabilities afforded by honeycomb-based SkXs.

Overall, these findings highlight the importance of lattice geometry and intrinsic magnetic parameters in controlling topological magnon transport. They establish theoretical foundations for experimental investigations and further explorations in the emerging field of 2D topological magnonics.

Acknowledgments

Part of the numerical calculations was performed using the Phoenix High Performance Computing facility at the American University of the Middle East (AUM), Kuwait.

References

- [1] S. A. Díaz, J. Klinovaja, and D. Loss, Topological Magnons and Edge States in Antiferromagnetic Skyrmion Crystals, *Phys Rev Lett* **122**, 187203 (2019).
- [2] T. Hirosawa, A. Mook, J. Klinovaja, and D. Loss, Magnetoelectric Cavity Magnonics in Skyrmion Crystals, *PRX Quantum* **3**, 040321 (2022).
- [3] T. Hirosawa, S. A. Diaz, J. Klinovaja, and D. Loss, Magnonic Quadrupole Topological Insulator in Antiskyrmion Crystals, *Phys Rev Lett* **125**, 207204 (2020).
- [4] S. A. Diáz, T. Hirosawa, J. Klinovaja, and D. Loss, Chiral magnonic edge states in ferromagnetic skyrmion crystals controlled by magnetic fields, *Phys Rev Res* **2**, 013231 (2020).
- [5] A. Roldán-Molina, A. S. Nunez, and J. Fernández-Rossier, Topological spin waves in the atomic-scale magnetic skyrmion crystal, *New J Phys* **18**, 045015 (2016).
- [6] D. Ghader and B. Jabakhanji, Momentum-space theory for topological magnons in two-dimensional ferromagnetic skyrmion lattices, *Phys Rev B* **110**, 184409 (2024).
- [7] K. Mæland and A. Sudbø, Quantum topological phase transitions in skyrmion crystals, *Phys Rev Res* **4**, L032025 (2022).
- [8] Z. Li, M. Ma, Z. Chen, K. Xie, and F. Ma, Interaction between magnon and skyrmion: Toward quantum magnonics, *J Appl Phys* **132**, 210702 (2022).
- [9] K. Mæland and A. Sudbø, Quantum fluctuations in the order parameter of quantum skyrmion crystals, *Phys Rev B* **105**, 224416 (2022).
- [10] V. E. Timofeev, Y. V. Baramygina, and D. N. Aristov, Magnon Topological Transition in Skyrmion Crystal, *JETP Lett* **118**, 911 (2023).
- [11] F. Zhuo, J. Kang, A. Manchon, and Z. Cheng, Topological Phases in Magnonics, *Advanced Physics Research* 2300054 (2023).
- [12] J. H. Han, J. Zang, Z. Yang, J. H. Park, and N. Nagaosa, Skyrmion lattice in a two-dimensional chiral magnet, *Phys Rev B Condens Matter Mater Phys* **82**, 094429 (2010).
- [13] S. Mühlbauer, B. Binz, F. Jonietz, C. Pfleiderer, A. Rosch, A. Neubauer, R. Georgii, and P. Böni, Skyrmion lattice in a chiral magnet, *Science* (1979) **323**, 915 (2009).
- [14] S. Heinze, K. Von Bergmann, M. Menzel, J. Brede, A. Kubetzka, R. Wiesendanger, G. Bihlmayer, and S. Blügel, Spontaneous atomic-scale magnetic skyrmion lattice in two dimensions, *Nature Physics* 2011 7:9 **7**, 713 (2011).
- [15] K. A. Van Hoogdalem, Y. Tserkovnyak, and D. Loss, Magnetic texture-induced thermal Hall effects, *Phys Rev B Condens Matter Mater Phys* **87**, 024402 (2013).
- [16] S. K. Kim, K. Nakata, D. Loss, and Y. Tserkovnyak, Tunable Magnonic Thermal Hall Effect in Skyrmion Crystal Phases of Ferrimagnets, *Phys Rev Lett* **122**, 057204 (2019).

- [17] T. Hirosawa, A. Mook, J. Klinovaja, and D. Loss, Magnetoelectric Cavity Magnonics in Skyrmiⁿ Crystals, *PRX Quantum* **3**, 040321 (2022).
- [18] T. Weber et al., Topological magnon band structure of emergent Landau levels in a skyrmion lattice, *Science* (1979) **375**, 1025 (2022).
- [19] M. Garst, J. Waizner, and D. Grundler, Collective spin excitations of helices and magnetic skyrmions: review and perspectives of magnonics in non-centrosymmetric magnets, *J Phys D Appl Phys* **50**, 293002 (2017).
- [20] O. Petrova and O. Tchernyshyov, Spin waves in a skyrmion crystal, *Phys Rev B Condens Matter Mater Phys* **84**, 214433 (2011).
- [21] M. Akazawa, H. Y. Lee, H. Takeda, Y. Fujima, Y. Tokunaga, T. H. Arima, J. H. Han, and M. Yamashita, Topological thermal Hall effect of magnons in magnetic skyrmion lattice, *Phys Rev Res* **4**, 043085 (2022).
- [22] V. E. Timofeev and D. N. Aristov, Magnon band structure of skyrmion crystals and stereographic projection approach, *Phys Rev B* **105**, 024422 (2022).
- [23] S. A. Owerre, A first theoretical realization of honeycomb topological magnon insulator, *Journal of Physics Condensed Matter* **28**, 386001 (2016).
- [24] L. Chen, J. H. Chung, B. Gao, T. Chen, M. B. Stone, A. I. Kolesnikov, Q. Huang, and P. Dai, Topological Spin Excitations in Honeycomb Ferromagnet CrI₃, *Phys Rev X* **8**, 041028 (2018).
- [25] L. Chen et al., Magnetic field effect on topological spin excitations in CrI₃, *Phys Rev X* **11**, 031047 (2021).
- [26] Z. Cai et al., Topological magnon insulator spin excitations in the two-dimensional ferromagnet CrBr₃, *Phys Rev B* **104**, L020402 (2021).
- [27] L. Chen et al., Magnetic anisotropy in ferromagnetic CrI₃, *Phys Rev B* **101**, 134418 (2020).
- [28] B. Huang et al., Layer-dependent ferromagnetism in a van der Waals crystal down to the monolayer limit, *Nature* **546**, 270 (2017).
- [29] C. Gong et al., Discovery of intrinsic ferromagnetism in two-dimensional van der Waals crystals, *Nature* **546**, 265 (2017).
- [30] Q. H. Wang et al., The Magnetic Genome of Two-Dimensional van der Waals Materials, *ACS Nano* **19**, 38 (2021).
- [31] D. Soriano, M. I. Katsnelson, and J. Fernández-Rossier, Magnetic Two-Dimensional Chromium Trihalides: A Theoretical Perspective, *Nano Lett* **20**, 6225 (2020).
- [32] K. S. Burch, D. Mandrus, and J.-G. Park, Magnetism in two-dimensional van der Waals materials, *Nature* **563**, 47 (2018).
- [33] S. Jiang, J. Shan, and K. F. Mak, Electric-field switching of two-dimensional van der Waals magnets, *Nat Mater* **17**, 406 (2018).

- [34] Z. Zhang, J. Shang, C. Jiang, A. Rasmita, W. Gao, and T. Yu, Direct Photoluminescence Probing of Ferromagnetism in Monolayer Two-Dimensional CrBr₃, *Nano Lett* **19**, 3138 (2019).
- [35] Y. Ahn, X. Guo, S. Son, Z. Sun, and L. Zhao, Progress and prospects in two-dimensional magnetism of van der Waals materials, *Prog Quantum Electron* **93**, 100498 (2024).
- [36] I. A. Verzhbitskiy, H. Kurebayashi, H. Cheng, J. Zhou, S. Khan, Y. P. Feng, and G. Eda, Controlling the magnetic anisotropy in Cr₂Ge₂Te₆ by electrostatic gating, *Nat Electron* **3**, 460 (2020).
- [37] W. Xing et al., Electric field effect in multilayer Cr₂Ge₂Te₆: a ferromagnetic 2D material, *2d Mater* **4**, 024009 (2017).
- [38] S. E. Nikitin, B. Fåk, K. W. Krämer, T. Fennell, B. Normand, A. M. Läuchli, and C. Rüegg, Thermal Evolution of Dirac Magnons in the Honeycomb Ferromagnet CrBr₃, *Phys Rev Lett* **129**, 127201 (2022).
- [39] G. Finocchio, F. Büttner, R. Tomasello, M. Carpentieri, and M. Kläui, Magnetic skyrmions: from fundamental to applications, *J Phys D Appl Phys* **49**, 423001 (2016).
- [40] F. Zhu et al., Topological magnon insulators in two-dimensional van der Waals ferromagnets CrSiTe₃ and CrGeTe₃: Toward intrinsic gap-tunability, *Sci Adv* **7**, 7532 (2021).
- [41] R. F. L. Evans, W. J. Fan, P. Chureemart, T. A. Ostler, M. O. A. Ellis, and R. W. Chantrell, Atomistic spin model simulations of magnetic nanomaterials, *Journal of Physics: Condensed Matter* **26**, 103202 (2014).
- [42] M. Ma, Z. Pan, and F. Ma, Artificial skyrmion in magnetic multilayers, *J Appl Phys* **132**, 043906 (2022).
- [43] Y. Li et al., An Artificial Skyrmion Platform with Robust Tunability in Synthetic Antiferromagnetic Multilayers, *Adv Funct Mater* **30**, 1907140 (2020).
- [44] B. Jabakhanji and D. Ghader, Designing Layered 2D Skyrmion Lattices in Moiré Magnetic Heterostructures, *Adv Mater Interfaces* **11**, 2300188 (2024).
- [45] A. Mook, J. Klinovaja, and D. Loss, Quantum damping of skyrmion crystal eigenmodes due to spontaneous quasiparticle decay, *Phys Rev Res* **2**, 033491 (2020).
- [46] J. Haraldsen and R. Fishman, Spin rotation technique for non-collinear magnetic systems: application to the generalized Villain model, *Journal of Physics: Condensed Matter* **21**, 216001 (2009).
- [47] J. H. P. Colpa, Diagonalization of the quadratic boson hamiltonian, *Physica A: Statistical Mechanics and Its Applications* **93**, 327 (1978).
- [48] T. Fukui, Y. Hatsugai, and H. Suzuki, Chern numbers in discretized Brillouin zone: Efficient method of computing (spin) Hall conductances, *J Physical Soc Japan* **74**, 1674 (2005).
- [49] D. Ghader, Magnon magic angles and tunable Hall conductivity in 2D twisted ferromagnetic bilayers, *Sci Rep* **10**, 15069 (2020).

- [50] Y. H. Li and R. Cheng, Moiré magnons in twisted bilayer magnets with collinear order, *Phys Rev B* **102**, 094404 (2020).
- [51] D. Ghader, Insights on magnon topology and valley-polarization in 2D bilayer quantum magnets, *New J Phys* **23**, 053022 (2021).